Applied Surface Science 465 (2019) 103–115

Contents lists available at ScienceDirect

Applied Surface Science

journal homepage: www.elsevier.com/locate/apsusc

Full Length Article

Construction of MIL-53(Fe) metal-organic framework modified by silver phosphate nanoparticles as a novel Z-scheme photocatalyst: Visible-light photocatalytic performance and mechanism investigation

Liangcheng Xie[a,b], Zhaohui Yang[a,b,*], Weiping Xiong[a,b], Yaoyu Zhou[c], Jiao Cao[a,b], Yanrong Peng[a,b], Xin Li[a,b], Chengyun Zhou[a,b], Rui Xu[a,b], Yanru Zhang[a,b]

[a] College of Environmental Science and Engineering, Hunan University, Changsha 410082, PR China
[b] Key Laboratory of Environmental Biology and Pollution Control (Hunan University), Ministry of Education, Changsha 410082, PR China
[c] College of Resources and Environment, Hunan Agricultural University, Changsha 410128, PR China

ARTICLE INFO

Keywords:
Photocatalysis
Ag_3PO_4/MIL-53(Fe)
Antibiotics
Visible light
Z-scheme

ABSTRACT

Novel heterostructure photocatalysts consisted of MIL-53(Fe) and silver phosphate (Ag_3PO_4) were successfully developed through a simple in situ precipitation strategy in this work. The photocatalytic activities of the as-synthesized samples were assessed via multiple antibiotics degradation, including tetracycline (TC), oxytetracycline (OTC), chlortetracycline (CTC) and deoxytetracycline (DCL). All the obtained Ag_3PO_4/MIL-53(Fe) composites exhibited much more superior photocatalytic activities than pure MIL-53(Fe) and Ag_3PO_4. Especially, the optimal composite with 1:3 mass ratio of Ag_3PO_4:MIL-53(Fe) (APM-3) displayed the best photocatalytic activity, for which the removal of antibiotics was 93.72% (TC), 90.12% (OTC), 85.54% (CTC) and 91.74% (DCL) under visible light irradiation for 1 h. The APM-3 also exhibited good photostability and recyclability. Three-dimensional (3D) EEMs (excitation-emission matrix fluorescence spectroscopy) was applied to further investigate the TC degradation process, and the TC intermediates were identified by high-performance liquid-mass spectrometry (HPLC-MS). The possible degradation pathway for TC was also discussed. In addition, electron spin resonance (ESR) measurement and quenching experiments verified that $^{\cdot}O_2^-$, $^{\cdot}OH$ and h^+ radicals all worked during the degradation process. In the end, a possible Z-scheme heterostructure model composed of MIL-53(Fe), metallic Ag and Ag_3PO_4 was proposed, in which the small reducible Ag nanoparticles functioned as a center for charge transmission. Powerful redox ability and effective separation of photoinduced carriers can be achieved in this Z-scheme heterostructure system. The findings of this work could offer a novel way to design MOF-based materials for remediation of contaminated water.

1. Introduction

Antibiotics have been widely used in our daily life since penicillin was produced in 1929 [1,2]. As persistent organic pollutants, antibiotics are considered to be a great threat to human health and aquatic ecosystems when entered into water body [3]. Therefore, environmental pollution of antibiotics has aroused increasing attention recently and various technique such as adsorption [4], electrochemical method [5,6], membrane separation [7] and photocatalysis [8,9] have been applied to eliminate it. Among these technologies, photocatalysis is viewed as one of the most desirable strategy due to its cost-effectiveness and high efficiency [10–12]. However, plenty of photocatalysts are limited in practical applications due to some drawbacks, such as poor light absorption capacity and stability, low quantum yield and rapid recombination of photoinduced electron-hole charges [13]. Hence, it is imperative to develop novel photocatalysts that have outstanding visible-light absorption and superior photoactivity.

Metal-organic frameworks (MOFs), a novel type of crystalline porous materials with high surface area, have attracted enormous attention recently [14]. In MOFs, metal ions or clusters are connected with organic ligands, and the ligand-to-metal charge transfer (LMCT) transitions make MOFs a new class of promising photocatalysts [15]. Since MOF-5 was first reported for phenol degradation upon light excitation [16], a large amount of studies have been concentrated on MOFs as photocatalysts for water splitting [17,18], CO_2 reduction [19,20] and organic pollutants degradation [21]. MIL-53(Fe), one of earth-abundant Fe(III)-based MOF constructed from Iron (III) chloride hexahydrate and 1,4-benzenedicarboxylic, stands out among numerous

* Corresponding author at: College of Environmental Science and Engineering, Hunan University, Changsha, Hunan 410082, PR China.
E-mail address: yzh@hnu.edu.cn (Z. Yang).

https://doi.org/10.1016/j.apsusc.2018.09.144
Received 25 May 2018; Received in revised form 17 August 2018; Accepted 17 September 2018
Available online 18 September 2018
0169-4332/

MOFs due to its semiconductor properties, visible light response, low cost and environment-friendly nature [22]. Du et al. successfully synthesized MIL-53(Fe) through a simple solvothermal approach and utilized it in MB removal under UV–vis and visible light illumination [23]. In Liang's research, MIL-53(Fe) exhibited considerable photocatalytic performance for the visible light degradation of dyes and reduction of Cr(VI) [24]. Nevertheless, the photocatalytic performance of pristine MIL-53(Fe) is still unsatisfied owing to the rapid recombination of electron-hole pairs. Over the years, many attempts have been paid to overcome the drawback. Oxidants including persulfate (PS) and hydrogen peroxide (H_2O_2) were adopted by researchers to improve the photocatalytic activity of bare MIL-53(Fe), which could act as electron acceptors participated in the photocatalytic system [25,26]. However, the amount of oxidants was comparatively large and the recyclability property of MIL-53(Fe) was likely to be influenced in most situations. Another popular method that coupling with other semiconductors to fabricate MIL-53(Fe)-based heterojunctions have been proved a good strategy, which can promote charge separation and transfer effectively. For instance, Huang et al. introduced g-C_3N_4 on the surface of MIL-53(Fe) then a g-C_3N_4/MIL-53(Fe) heterojunction was developed, which greatly boosted the separation of photoexcited electron-hole charges [27]. Hu et al. also fabricated heterojunction photocatalysts based on CdS and MIL-53(Fe), and remarkably improved photocatalytic properties were obtained [28]. For the better development and deeper investigation, it is expected that more novel MIL-53(Fe)-based heterostructured photocatalysts should be constructed.

Generally in the typical charge transfer heterostructure, the redox ability of the photoinduced charges would be weakened after charge transmission, which was unfavourable for the photocatalytic activity [29]. Nowadays, Z-scheme heterostructure constructed by two matchable band gap semiconductors has become a research hotspot, which can achieve enhanced charge carriers' separation efficiency thanks to the internal charge transmission [30]. The stronger oxidization ability of holes gathered on a more positive valence band (VB) as well as powerful reduction ability of electrons accumulated on a more negative conduction band (CB) could be utilized in the Z-scheme system. Therefore, it is of great enthusiasm to fabricate MIL-53(Fe)-based Z-scheme heterostructures. Accordingly, various studies had demonstrated that coupling Ag compounds photocatalysts and other semiconductors with suitable band-gap is very likely to develop Z-scheme structure, such as AgI/$BiVO_4$ [31], AgI/Bi_5O_7I [32] and Ag_3PO_4/g-C_3N_4 [30].

Silver phosphate (Ag_3PO_4), an attractive semiconductor photocatalyst with high quantum efficiency under visible light irradiation, displayed wonderful photocatalytic activity in water splitting and organic pollutant elimination [33]. Unfortunately, when Ag_3PO_4 was exposed to light, the Ag^+ can react with electrons then reduced into metallic Ag, which could dramatically decrease its photocatalytic activity. The practical application of Ag_3PO_4 was hindered due to severe photocorrosion. The key to solve the problem is to transfer and separate the photogenerated electrons and holes timely. Therefore, large amounts of efforts have been put into improving the anti-photocorrosion performance of Ag_3PO_4, and establishing Z-scheme heterojunction structure based on Ag_3PO_4 and other appropriate band-gap semiconductors has been proven an effective method more recently [34]. For example, Cai et al. designed a well- fabricated Z-scheme system consisted of La, Cr-codoped $SrTiO_3$ and Ag_3PO_4@RGO, both excellent anti-photocorrosion performances and improved photoactivity realized [35]. Interestingly, Yan et al. successfully constructed a Z-scheme heterostructure through combining Ag_3PO_4 with In_2S_3, where electrons from Ag_3PO_4 can be transported to Ag and finally recombined with holes from In_2S_3, contributing to the inhibition of the photocorrosion of both In_2S_3 and Ag_3PO_4 [36]. However, there are no related studies devoted to building the Z-scheme structure on the basis of MIL-53(Fe) and Ag_3PO_4.

Herein, this study reported the fabrication of Ag_3PO_4/MIL-53(Fe) for the first time, and Ag_3PO_4 nanoparticles were successfully adhered to the surface of MIL-53(Fe) through a facile in situ precipitation approach. The photocatalytic performances of the obtained photocatalysts were assessed towards the visible-light degradation of multiple antibiotics, including TC, OTC, CTC and DCL. The results demonstrated that Ag_3PO_4 loading obviously enhanced the photocatalytic property of MIL-53(Fe). The effect of initial TC concentration was taken into discussion, and 3D EEMs was applied to make further investigation on the mineralization ability of the Ag_3PO_4/MIL-53(Fe) hybrids towards the TC degradation. TC intermediates and the possible degradation pathways were studied through LC-MS analysis. Moreover, the photocatalytic stability of Ag_3PO_4 and APM-3 was evaluated after four successive cycles. The photoinduced charge transport and separation ability of the obtained samples was also investigated. Quenching experiments and ESR tests were employed to identify the major active groups participated in the photodegradation reaction. Ultimately, a possible Z-scheme model was proposed in detail.

2. Experimental section

2.1. Chemicals and reagents

$FeCl_3{\cdot}6H_2O$, 1,4-benzenedicarboxylic (H_2BDC), N,N-dimethylformamide (DMF), silver nitrate($AgNO_3$), disodium hydrogen phosphate (Na_2HPO_4), ethanol (CH_3CH_2OH), tetracycline (TC), deoxytetracycline (DCL), oxytetracycline (OTC), chlortetracycline (CTC) were purchased from Sinopharm Chemical Reagent Co. Ltd (Shanghai, China). All reagents and solvents used in this experiment have not been further purified and were analytical grade.

2.2. Synthesis of MIL-53(Fe)

According to the previous report, a facile solvothermal approach was adopted to prepare MIL-53(Fe) [37]. In a typical procedure, a mixture of $FeCl_3{\cdot}6H_2O$, H_2BDC, DMF (with a molar ratio of 1:1:280) was stirred mechanically at room temperature until it turned into a transparent solution. Next the solution was maintained at 150 °C for 15 h after poured into a Teflon-lined stainless steel autoclave. The resulting sample was collected by centrifugation after the autoclave cooled naturally to room temperature, and washed several times with DMF and C_2H_5OH, respectively. Subsequently, the product was suspended in 200 mL of distilled water overnight so that the guest molecules in the pores could be removed. Then the collected powder was dried in vacuum at 60 °C overnight.

2.3. Synthesis of Ag_3PO_4/MIL-53(Fe)

The Ag_3PO_4/MIL-53(Fe) hybrids were obtained through a simple precipitation method as follows. Firstly, a given mass of MIL-53(Fe) was dispersed into 50 mL deionized water under sonication treatment for 30 min. Following 0.9 mmol $AgNO_3$ was added into the above mixture and stirred under dark condition for 30 min. Next, 20 mL solution containing 0.3 mmol Na_2HPO_4 was added gradually, and the obtained mixture was stirred vigorously in dark for 12 h. The resultant sample was collected via filtration, washed with deionized water and C_2H_5OH, and dried at 60 °C under vacuum. By changing the amount of MIL-53(Fe), Ag_3PO_4/MIL-53(Fe) hybrids with different mass ratio (Ag_3PO_4:MIL-53(Fe) = 1:1, 1:3, 1:5), denoted as APM-1, APM-3, APM-5 were obtained. Similarly, bare Ag_3PO_4 was obtained without the addition of MIL-53(Fe) under the same process.

2.4. Characterization

The crystalline nature of photocatalysts was confirmed by powder X-ray diffraction (XRD) technique with a Bruker AXS D8 Advance X-ray diffractometer in the range from 10° to 60°. Fourier transformed

infrared (FTIR) spectra were recorded on BioRad FTS 6000 spectrometer. X-ray photoelectron spectra (XPS) of the samples were performed on ESCALAB 250XI spectrometer (Thermo Fisher, USA). The morphology of the samples was investigated by scanning electron microscopy (SEM, Hitachi S-4800) and transmission electron microscopy (TEM, Tecnai G2 F20) was used to characterize the microstructures. The Brunauer-Emmett-Teller (BET) surface area test was carried out by a TRISTAR-3000 surface area analyzer at 77 K. The thermal decomposition behavior of samples was tested by thermogravimetric analysis (TGA) (TA Q500, America) with a heating rate of 10 °C min^{-1} under N_2 atmosphere. The UV–vis diffuse reflectance spectra (UV–vis DRS) were examined in a range of 200–800 nm by a UV–vis spectrophotometer (Hitachi U-3310). 3D EEMs were performed on fluorescence spectrophotometer (FluoroMax-4). The intermediates of TC were tested by a LC-MS/MS system (1290/6460 Triple Quad, Agilent) and the details were illustrated in the supplementary material. PL spectra were tested by F-7000 fluorescence spectrometer. The electron spin resonance (ESR) signals of radicals were examined on Bruker ER200-SRC spectrometer under visible light irradiation (λ > 420 nm).

2.5. Photocatalytic experiments

The photocatalytic degradation experiments were performed under a 300 W Xe lamp (CEL-HXF300, Beijing, China) with a 420 nm cutoff filter. Briefly, 50 mg photocatalyst was mixed with 100 mL of TC (20 mg L^{-1}), OTC (20 mg L^{-1}), CTC (20 mg L^{-1}), or DCL (20 mg L^{-1}). To reach adsorption-desorption equilibrium, the solution was stirred in dark for 1 h before illumination. During the irradiation process, 4 mL of solution was taken out at a given time interval, then centrifuged. The corresponding concentrations of TC, OTC, CTC, DCL were analyzed with a Shimadzu UV–vis spectrophotometer at their characteristic wavelengths of 357 nm, 352 nm, 366 nm, and 346 nm, respectively.

2.6. Photo-electrochemical measurements

A typical three-electrode system based on a CHI-660D electrochemical workstation was employed to measure the photoelectrochemical characteristics of the obtained samples. The reference electrode was provided by an Ag/AgCl electrode in saturated KCl solution while the counter electrode was offered by a Pt electrode. The photocurrent tests and electrochemical impedance spectroscopy (EIS) measurements were conducted based on the above three-electrode system with Na_2SO_4 solution (0.2 M) as electrolyte solution. A 300 W Xe lamp with a cut-off filter (λ > 420 nm) served as the light source.

3. Results and discussion

3.1. Catalyst characterization

The crystalline nature and composition of MIL-53(Fe), Ag_3PO_4 and Ag_3PO_4/MIL-53(Fe) composites were investigated by XRD. As displayed in Fig. 1a, the XRD pattern of bare MIL-53(Fe) was consistent with the simulated one as well as the previous reports [38,39]. And the diffraction peaks were sharp, indicating high crystallinity. The diffraction pattern for prepared Ag_3PO_4 displayed nine distinct peaks at 20.9°, 29.7°, 33.3°, 36.5°, 42.5°, 47.8°, 52.6°, 55.0° and 57.3°, which can be related to the (1 1 0), (2 0 0), (2 1 0), (2 1 1), (2 2 0), (3 1 0), (2 2 2), (3 2 0) and (3 2 1) planes of the body-centered cubic structure of Ag_3PO_4 (JCPDS No. 06-0505), respectively [29]. All the patterns of Ag_3PO_4/MIL-53(Fe) hybrids exhibited the characteristic peaks of both Ag_3PO_4 and MIL-53(Fe), suggesting the successful combination of Ag_3PO_4 and MIL-53(Fe). Moreover, the intensities of diffraction peaks for MIL-53(Fe) enhanced as the mass ratios increased, which was in good accordance with the rising MIL-53(Fe) amounts in the synthesis process. And no shift in the characteristic peak positions of MIL-53(Fe) was observed in the patterns of Ag_3PO_4/MIL-53(Fe) composites,

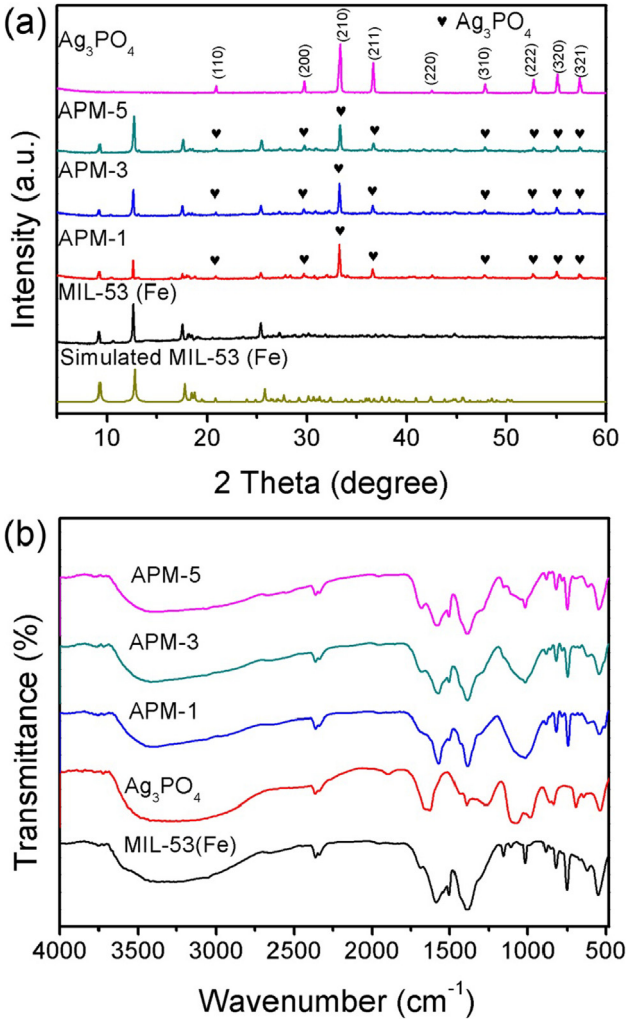

Fig. 1. (a) XRD patterns, (b) FTIR spectra of MIL-53(Fe), Ag_3PO_4 and Ag_3PO_4/MIL-53(Fe) composites.

implying that the crystal structure of MIL-53(Fe) was not destroyed by the introduction of Ag_3PO_4.

FT-IR spectroscopy was applied to provide detail information of the molecular structure and functional groups. Fig. 1b showed the FT-IR spectra of MIL-53(Fe), Ag_3PO_4, and Ag_3PO_4/MIL-53(Fe) heterojunction samples. Five absorption peaks located at 1691, 1573, 1388, 750, 546 cm^{-1} can be observed in the spectrum of MIL-53(Fe). The peak at 1691 cm^{-1} correspond to C=O stretching mode [25]. The absorption bands observed at 1388 and 1573 cm^{-1} could be ascribed to symmetric and asymmetric vibrations of carboxyl groups, respectively [40]. And the absorption peak of C−H bonding vibrations in the benzene rings can be observed at 750 cm^{-1} [41]. In addition, the peak at 546 cm^{-1} was assigned to the stretching vibration of Fe−O bonds [42]. As for the FT-IR spectrum of pure Ag_3PO_4, three peaks presented at 542 cm^{-1}, 986 cm^{-1} and 1074 cm^{-1} can be ascribed to O=P−O flexural vibrations, asymmetric stretching of the P−O bonds and P−O stretching vibrations of PO_4^{3-}, respectively [35,43]. The characteristic peaks of MIL-53(Fe) and Ag_3PO_4 were obtained in the Ag_3PO_4/MIL-53(Fe) hybrid composites, demonstrating successful fabrication of Ag_3PO_4/MIL-53(Fe) to a certain extent.

The surface composition and chemical states of APM-3 was further investigated by XPS technique. Peaks corresponding to C, O, Fe, Ag and P elements were displayed in the survey spectra (Fig. 2a), which was in accord with the composition of APM-3. Moreover, Fig. S1 presented the survey spectra of MIL-53(Fe) and Ag_3PO_4. The high resolution XPS C 1s

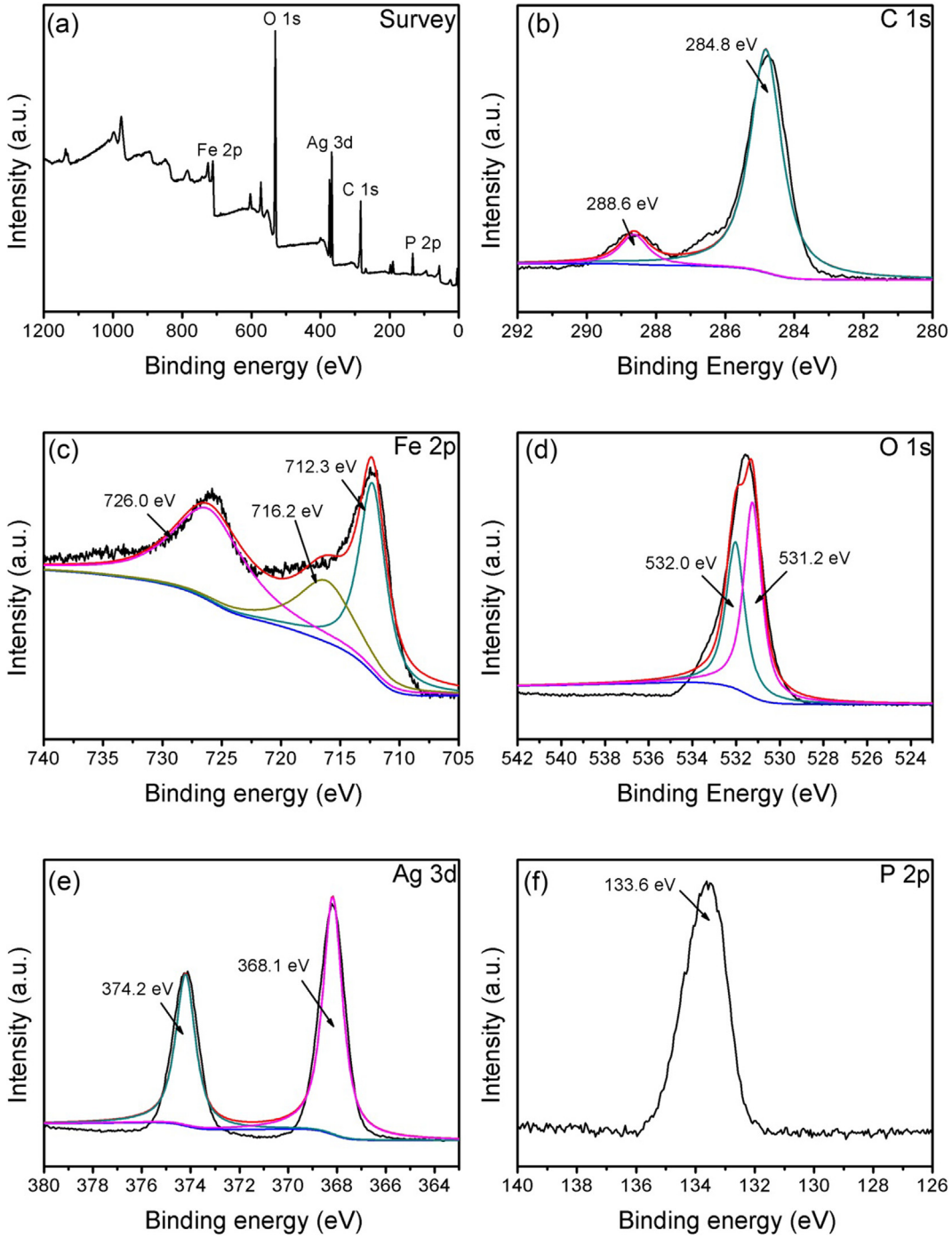

Fig. 2. The XPS spectra of APM-3: (a) survey spectra, (b) C 1s, (c) Fe 2p, (d) O 1s, (e) Ag 3d and (f) P 2p.

spectrum in Fig. 2b could be fitted into two peaks centered at 284.8 eV and 288.6 eV, corresponding to benzoic rings and the carboxylate (O—C═O) groups of H_2BDC, respectively [44]. In the Fe 2p XPS spectrum (Fig. 2c), the peak at 712.3 eV can be attributed to Fe $2p_{3/2}$ while the peak at 726.0 eV can be assigned to Fe $2p_{1/2}$. And the peak separation was approximately 13.7 eV, which was consistent with those reported for α-Fe_2O_3 [45]. Besides, a satellite signal at 716.2 eV was displayed [46]. The above results confirmed that Fe^{3+} existed in the APM-3 structure. The O 1s spectrum in Fig. 2d could be divided into two peaks. The peak at 532.0 eV was related to the oxygen components of the H_2BDC, and the other peak at 531.2 eV was indexed to the Fe—O bonds of MIL-53(Fe) and the oxygen in the Ag_3PO_4 crystal lattice [36,47]. Fig. 2e showed the spectrum of Ag 3d in APM-3, where two peaks located at 368.1 and 374.2 eV could be ascribed to Ag $3d_{5/2}$ and Ag $3d_{3/2}$ of Ag^+ in Ag_3PO_4, respectively [30]. No other peaks corresponded to Ag^0 can be found, the result confirmed that no metallic Ag was generated in the preparation procedure of APM-3 sample. Moreover, Fig. 2f showed the P 2p spectrum with a peak at 133.6 eV, which demonstrated that the valence state of P was +5 in the APM-3 composite [48].

SEM was adopted to study the morphology and size of the as-synthesized samples. As can be seen from Fig. 3a and d, MIL-53(Fe) exhibited a rhombic polyhedron morphology with smooth surface, and the length was about 3–4 μm. After decorated with Ag_3PO_4, the surface of MIL-53(Fe) became coarse and some nanoparticles can be observed on it (Fig. 3b and e). The TEM instrument was applied to assist the SEM

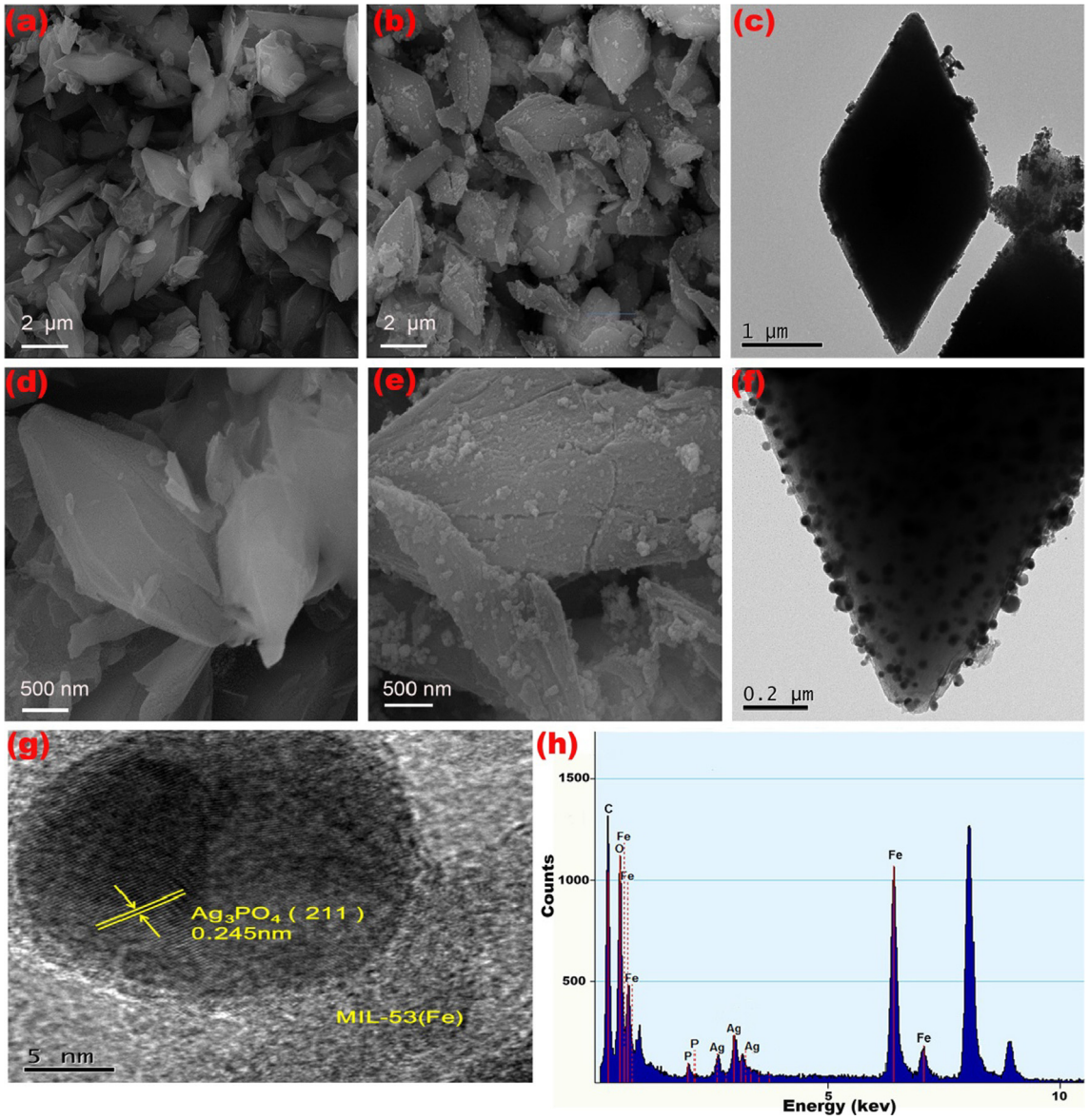

Fig. 3. (a and d) SEM images of MIL-53(Fe); (b and e) APM-3 samples; (c and f) TEM images of APM-3; (g) HRTEM image of APM-3; (h) EDX analysis of APM-3.

analysis. From the Fig. 3c and f, it can be clearly seen that Ag_3PO_4 nanoparticles were anchored on the surface of MIL-53(Fe) intimately, and the introduction of Ag_3PO_4 did not change the main morphology of MIL-53(Fe). In addition, HRTEM image of APM-3 was also provided. As exhibited in Fig. 3g, the lattice distance of 0.245 nm indexed to the (2 1 1) plane of Ag_3PO_4 [29], demonstrating that Ag_3PO_4 was successfully decorated on the surface of MIL-53(Fe). These results were the solid evidences for the successful construction of Ag_3PO_4/MIL-53(Fe) heterojunction structure, which could promote the separation of the photoexcited electron-hole charges to enhance the photocatalytic activity. Moreover, the existence of C, Fe, O, Ag and P elements in the APM-3 composite was further confirmed through the energy dispersive X-ray spectrometry (EDX) spectrum displayed in Fig. 3h.

Fig. 4a illustrated the N_2 adsorption-desorption isotherms of pure MIL-53(Fe) and APM-3 composite and the relevant calculated parameters were presented in Table 1. Both of the samples were of type IV isotherm with a type H3 hysteresis loop, indicating the existence of mesopores. The BET surface area of MIL-53(Fe) was 8.531 $m^2 g^{-1}$, which was similar to the previous report [49]. Compared with pure MIL-53(Fe), APM-3 exhibited a larger surface area (15.525 $m^2 g^{-1}$), pore size (6.792 nm) and pore volume (0.097 $cm^3 g^{-1}$). Generally, high specific surface area was favorable for the reactants adsorption and active sites production, which can make contribution to the photocatalytic performance.

In addition, the thermal decomposition behavior of the APM-3, APM-3 collected after TC adsorption and photocatalytic degradation process was studied by thermogravimetric analysis (TGA). As presented in Fig. S3, the as-synthesized APM-3 had lost weight in several steps. The weight-loss stage below 300 °C was attributed to the loss of guest solvent molecules and water [50]. Next the sharp weight loss occurred between 300 °C and 550 °C was caused by the elimination of the organic ligands within the framework [51]. And the weight of APM-3 was still decreasing above 600 °C, which was associated with the complete decomposition of the framework [52]. As for the APM-3 collected after TC adsorption process, three weight-loss stage between room temperature and 600 °C was exhibited in the TG curve. At the first stage, solvents including DMF and water were removed below 200 °C. Then an obvious weight loss occurred between 200 °C and 320 °C, which was different from that of APM-3. It was probably due to the decomposition of the TC molecules adsorbed by APM-3. Previous studies also reported that TC molecules begin to break down around 200 °C [53]. The third weight loss at 320–600 °C was owing to the destruction of H_2BDC links within

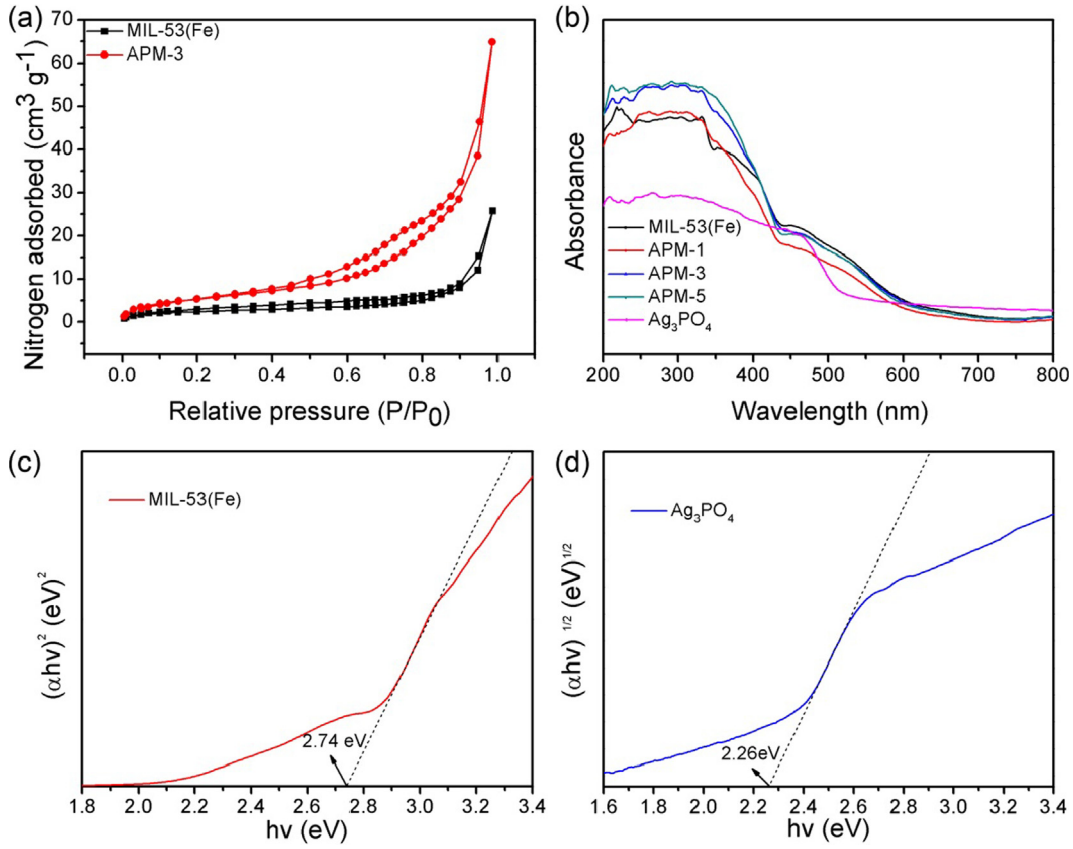

Fig. 4. (a) Nitrogen adsorption-desorption isotherm of the as-prepared MIL-53(Fe) and APM-3 composite, (b) DRS spectra of MIL-53(Fe), Ag_3PO_4 and Ag_3PO_4/MIL-53(Fe) composites, (c and d) band gap energies of MIL-53(Fe) and Ag_3PO_4, respectively.

Table 1
Surface area, pore size and pore volume parameters for pure MIL-53(Fe) and APM-3 composite.

Samples	Surface area ($m^2 g^{-1}$)	Pore size (nm)	V_t ($cm^3 g^{-1}$)
MIL-53(Fe)	8.531	3.409	0.040
APM-3	15.525	6.792	0.097

the framework. Moreover, the TG curve of the APM-3 collected after photodegradation process displayed similar trends as that of APM-3, suggesting that TC molecules adsorbed by APM-3 had been further photocatalytic degraded.

To analyze the absorption capability and optical bandgap of the obtained samples, UV/vis diffuse reflectance spectrum (DRS) was used. As presented in Fig. 4b, MIL-53(Fe), Ag_3PO_4 and Ag_3PO_4/MIL-53(Fe) hybrids all exhibited good absorption in the visible light range. For the spectrum of pure MIL-53(Fe), the little peak located at 445 nm could be owing to the spin-allowed d-d transition ($^6A_{1g} \rightarrow {}^4A_{1g} + {}^4E_g(G)$) in Fe (III) [26,54]. When Ag_3PO_4 was introduced into the surface of MIL-53(Fe), all hybrids displayed an enhanced absorption in the range of 480–580 nm compared with that of Ag_3PO_4. An optical property parameter to evaluate the production and transfer of photoinduced charges was the bandgap edge (E_g) of the semiconductor, which can be calculated through the following formula:

$$\alpha h\nu = A(h\nu - E_g)^{n/2} \quad (1)$$

where α, h, A, ν and E_g are absorption coefficient, Plank constant, a proportionality constant, light frequency and optical band gap, respectively. And n is determined by the type of optical transition in the semiconductor (n = 4 for an indirect transition while n = 1 for a direct transition) [55]. MIL-53(Fe) belong to the direct band semiconductor, while Ag_3PO_4 is regarded as an indirect transition semiconductor. The band gap energy of the semiconductors could be obtained according to the X-intercept of the tangent line. As depicted in Fig. 4c and Fig. 4d, the E_g values of MIL-53(Fe) and Ag_3PO_4 were approximately 2.74 and 2.26 eV, respectively, the values were in good agreement with the previous reports [55,56].

3.2. Photocatalytic activities

The photocatalytic performance of all the obtained photocatalysts was accessed via multiple antibiotics degradation. In our experiment, TC, OTC, CTC, DCL were selected as the target pollutants. As shown in Fig. 5a, no obvious change of degradation efficiency can be observed in blank experiments without photocatalyst, suggesting that the photolysis effect of TC was negligible. Pure MIL-53(Fe) displayed poor photocatalytic performance, and the removal of TC was only 26.45% within 60 min irradiation. Furthermore, for single Ag_3PO_4, it could remove about 71.67% of TC under the identical conditions. The hybrid composites showed higher photocatalytic performance compared with the pristine samples, where the removal efficiencies of TC were about 89.95%, 93.72%, 82.06% for APM-1, APM-3, APM-5, respectively. Obviously, the APM-3 exhibited the most superior photocatalytic performance in all of the samples. The better photocatalytic activity of Ag_3PO_4/MIL-53(Fe) samples should be ascribed to the forming heterojunction between Ag_3PO_4 and MIL-53(Fe), which can facilitate the effective separation of photoinduced charge carries during the reaction process. The loading of Ag_3PO_4 in Ag_3PO_4/MIL-53(Fe) composites may form more active sites for photocatalytic reaction, while excessive loading amount of Ag_3PO_4 might lead to an agglomeration phenomenon and the area exposed to the incoming light would be reduced, thus the decreased photocatalytic efficiency was displayed. The removal of OTC, CTC, and DCL was identical with that of TC, and the relevant

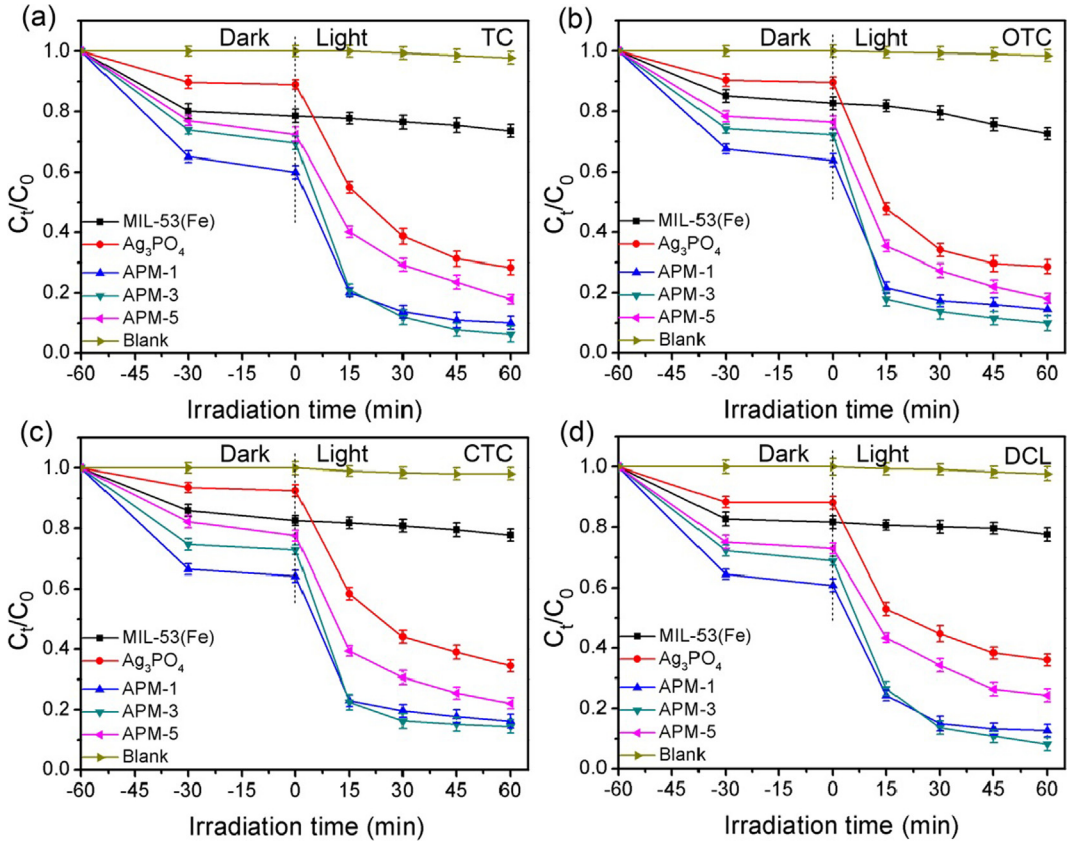

Fig. 5. Photocatalytic degradation of (a) TC, (b) OTC, (c) CTC, and (d) DCL by as-prepared samples under visible light irradiation.

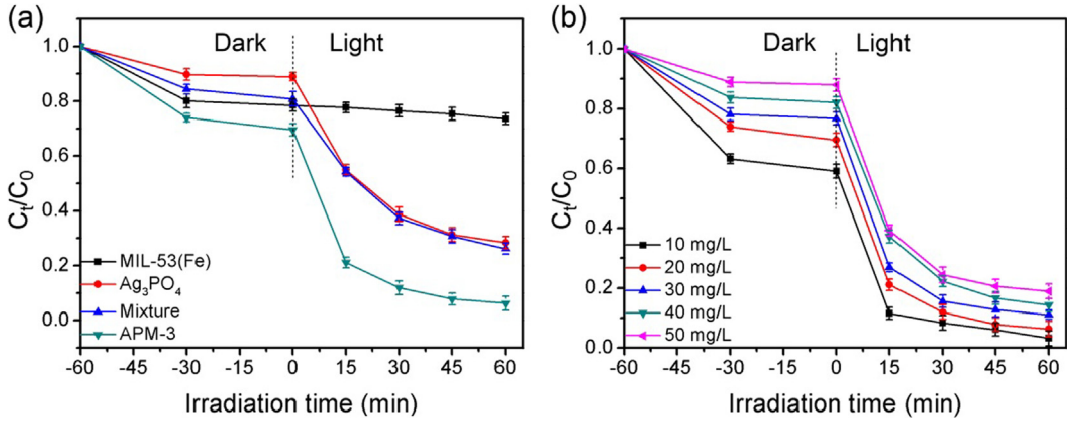

Fig. 6. (a) Photocatalytic degradation of TC by different samples, (b) Effects of the initial concentration of TC on the photocatalytic activities in presence of APM-3.

removal rate for different samples can be ranked as follows: MIL-53(Fe) < Ag_3PO_4 < APM-5 < APM-1 < APM-3. Notably, the removal of OTC, CTC and DCL by APM-3 improved 62.64% (Fig. 5b), 63.28% (Fig. 5c), and 69.40% (Fig. 5d) compared with MIL-53(Fe), respectively. Furthermore, the photocatalytic performance of physically mixed was also inspected. As shown in Fig. 6a, the removal of TC over the mixture (with mass ratio of Ag_3PO_4:MIL-53(Fe) = 1:3) was 73.79%, which was much lower than that of APM-3 composite. The result further confirmed the heterojunction construction between Ag_3PO_4 and MIL-53(Fe).

In practice, the concentration of pollutants may vary greatly. So, it is worthwhile to inspect the impact of initial contaminant concentration on the performance of photocatalysts. As presented in Fig. 6b, various initial concentrations of TC (10, 20, 30, 40, 50 mg L^{-1}) were provided to evaluate the photoactivity of APM-3. Negative effect can be observed with the increasing TC concentrations, which could be explained by the following two aspects: (a) longer pathway for photons entering the TC solution and fewer photons arriving at the surface of the photocatalysts in higher concentration; (b) stronger competition between pollutants and intermediates existed in high pollutant concentration, consequently caused reduced contact between TC molecules and photocatalyst [31]. It is worth noting that only 15.75% reduction of TC degradation efficiency was obtained, from 96.80% (10 mg L^{-1}) to 81.05% (50 mg L^{-1}), demonstrating that APM-3 have great potential in TC or other pollutants treatment even at a comparatively higher concentration.

3D EEMs can inspect the TC degradation and could reflect the mineralization ability of a photocatalyst to some degree [57]. The fluorescence spectra parameters were shown in Table S1. As depicted in Fig. 7a and b, no florescence signal was observed in the original solution and the solution collected after adsorption for 60 min,

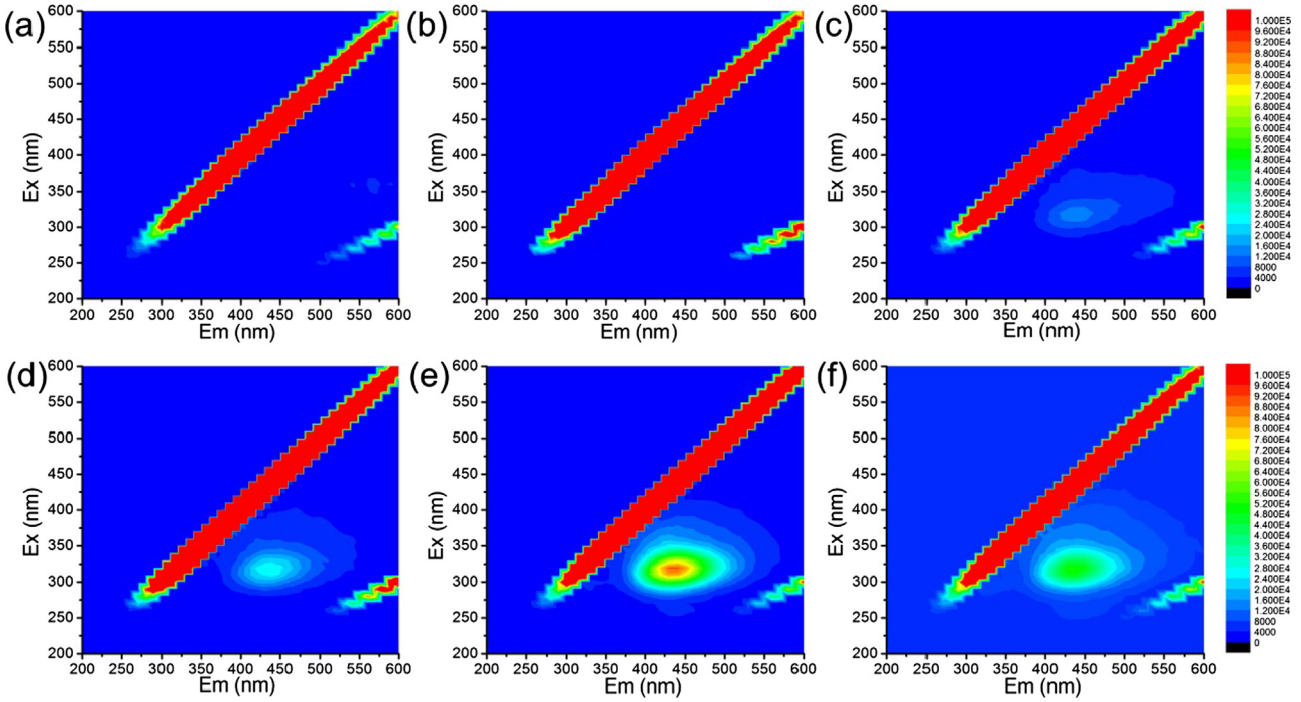

Fig. 7. 3D EEMs of the aqueous solution: (a) taken from the original solution; (b) collected after 60 min adsorption in dark; (c–f) obtained after an irradiation time of 15, 30, 60, and 120 min, respectively.

demonstrating that TC molecule was not turned into other products under dark condition. Under visible light irradiation, one fluorescence peak centered at Ex/Em = (305–330 nm)/(430–450 nm) appeared (Fig. 7c–f), which was a signal for TC degradation and was in agreement with previous research reported by Chen et al. [32]. The characteristic peak can be ascribed to the humic acids-like fluorescence region [58]. Moreover, it could be observed that the fluorescence signal increased with the illumination time from 15 min to 60 min (Fig. 7c–e), suggesting that TC was decomposed gradually. However, the fluorescence intensity reduced obviously upon the illumination time reached to 120 min, indicating the degradation of humic acids-like matter and partial mineralization of TC molecules into CO_2 and H_2O.

High-performance liquid-mass spectrometry (HPLC-MS) was employed to identify the TC intermediates during the degradation process. The MS spectra of main intermediates were shown in Fig. S4. The single peak with the mass-to-charge ratio (m/z) of 445.2 can be directly observed in original TC solution (Fig. S4a), and the intensity of the peak for TC was decreased after 60 min adsorption (Fig. S4b). Based on the previous reports and the detected degradation products, the possible degradation pathway for TC has been proposed as illustrated in Fig. 8. Firstly, TC 1 (m/z = 461) was produced through hydroxylation of TC, while TC 2 (m/z = 459) was generated by multiple hydroxylation reactions and the loss of water at carbon ring [58,59]. Then TC 2 was transformed to TC 3 (m/z = 362) via a deamidation process, the loss of hydroxyl and methyl groups, and hydroxyl-substitution reaction due to the attack of $^{\cdot}OH$ radicals [60,61]. Similarly, TC 1 also can be converted to TC 3 by a series of reactions. According to Chen's study, TC 4(m/z = 318) was originated from the decomposition of TC 3 by the breakage of the carboatomic ring [62]. And TC 4 can be further transformed to TC 5 (m/z = 274) via the decarboxylation process. TC 6 (m/z = 261) was stemmed from TC 5 through the loss of methyl group and hydrogenation. Afterwards, TC 6 might undergo a dehydroxymethylation process to yield TC 7 (m/z = 230) [63]. Furthermore, TC 8 with m/z value of 209 was also detected, which could be considered as the opening ring product of TC 7. Finally, the intermediates were further mineralized into CO_2 and H_2O. Therefore, the intermediates during the photocatalytic degradation reaction were produced through two main routes: the ring-opening reactions and the loss of functional groups.

Except for the high removal efficiency, the stability and recyclability properties of one photocatalyst were also significant in practical application. Hence, the repeated experiments were performed on Ag_3PO_4 and APM-3 composite for TC degradation. After each run of photocatalytic reaction, the catalyst was gathered via filtration, washed, then dried and used again to start a new cycle. As displayed in Fig. 9a, an obvious decrease of the TC removal efficiency was observed for pure Ag_3PO_4, from 71.67% to 46.46% after four recycling runs. However, only 8.12% degradation efficiency loss at the fourth run was detected in the APM-3 sample, which was much less than that of Ag_3PO_4 (25.21% loss). The results demonstrated that APM-3 obtained not only much higher photocatalytic performance than pure MIL-53(Fe) but also much higher photocatalytic degradation stability than pure Ag_3PO_4. Moreover, the XRD patterns of the used Ag_3PO_4 and APM-3 were presented in Fig. 9b. Two new diffraction peaks located at 38.1° and 44.3° corresponding to the (1 1 1) plane and (2 0 0) plane of metallic Ag (JCPDS card no. 65-2871), respectively, were observed for used Ag_3PO_4 clearly [64], while only a weak peak at 38.1° was appeared in the APM-3 compared with the fresh sample and the intensity value was much lower than that of used Ag_3PO_4. The result further confirmed that metallic Ag was easily generated when Ag_3PO_4 was under visible light illumination, as a result, Ag_3PO_4 suffered from photocorrosion seriously, but APM-3 could avoid the photocorrosion problem effectively to a certain extent.

3.3. Photocatalytic mechanism study

The trapping experiments have been performed to explore the photocatalytic mechanism. In this study, $^{\cdot}O_2^-$, holes and $^{\cdot}OH$ were trapped by three different scavengers, 1.4-benzoquinone (BQ), $Na_2C_2O_4$ and isopropanol (IPA), respectively [65,66]. As shown in Fig. 10a, When $Na_2C_2O_4$ and BQ were added to the photocatalytic procedure, the degradation efficiency for TC was remarkably decreased from 93.72% to 48.46% and 64.95%, respectively, demonstrating that h^+ and $^{\cdot}O_2^-$ took a crucial part in the TC degradation. Besides, less decrease of TC

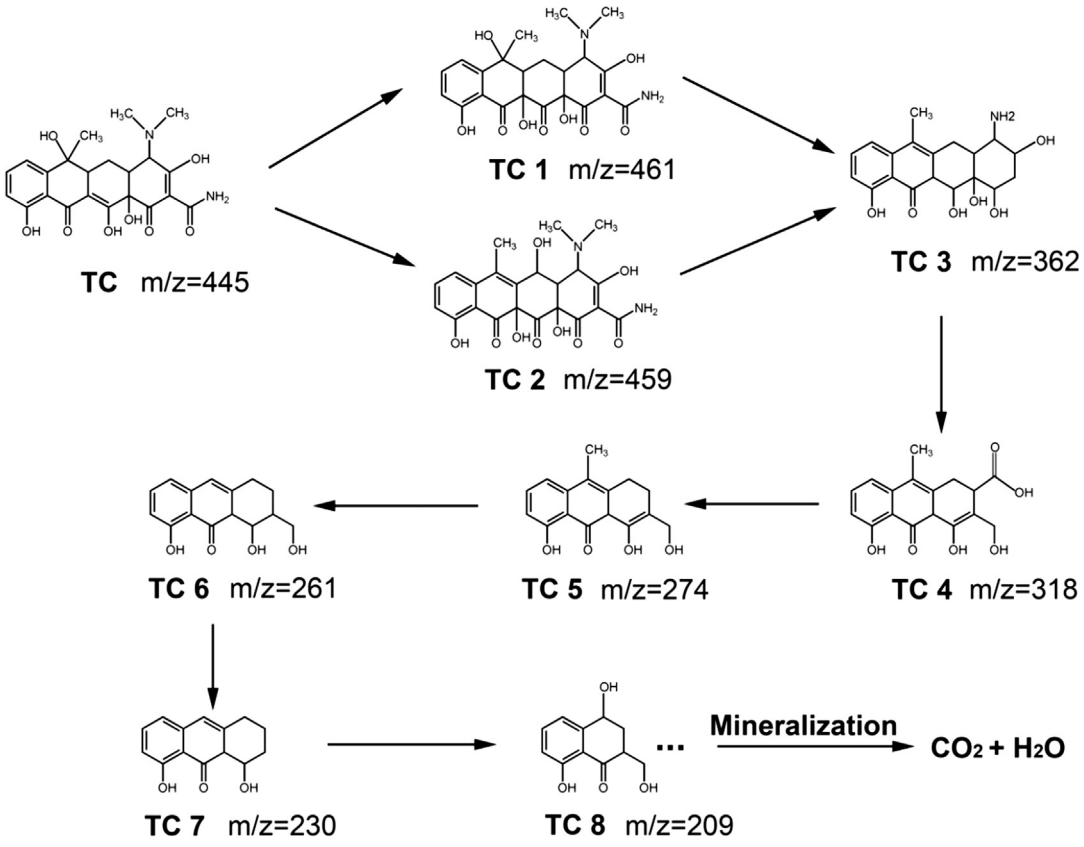

Fig. 8. Suggested pathways for the photodegradation of TC.

degradation efficiency was observed by the addition of IPA, indicating ·OH was also responsible for degradation process.

To further confirm the above-obtained radicals were generated upon visible light excitation in the presence of APM-3 composite, the ESR spectra of free radicals and holes captured by DMPO ($\cdot O_2^-$ and ·OH) and TEMPO (h^+) were provided. As presented in Fig. 10b, four peaks for $\cdot O_2^-$ were detected in methanol dispersion after the light was turned on while no signal was found in dark condition, proving that $\cdot O_2^-$ was generated during the reaction procedure. Simultaneously, with the irradiation time increased, an increasing intensity for DMPO-$\cdot O_2^-$ signals can be obtained, indicating that more $\cdot O_2^-$ radicals were formed in the degradation system. Similarly, it can be observed that the intensity of DMPO-·OH signals was increased gradually from Fig. 10c, demonstrating that ·OH radicals also existed in APM-3 reaction system. Moreover, test for photo-induced holes (h^+) was also applied. As displayed in Fig. 10d, the signal of spin-trapped TEMPO-h^+ was detected in dark condition, but stronger intensity was presented when APM-3 sample exposed to visible light, demonstrating that h^+ worked in the photocatalytic process. The above results were in good accordance with the radical trapping experiment.

Photoluminescence (PL) spectroscopy was applied to inspect the separation efficiency of charge carriers in semiconductor photocatalysts. Generally, lower fluorescence intensity suggested the more efficient charge separation [13]. Fig. 11a presented the PL spectra of MIL-53(Fe), Ag_3PO_4 and APM-3 with the excitation wavelength of 437 nm. As we can see, three samples exhibit similar shapes with an emission peak at about 482 nm. Both pure MIL-53(Fe) and Ag_3PO_4 obtained a high PL intensity, which was caused by the rapid

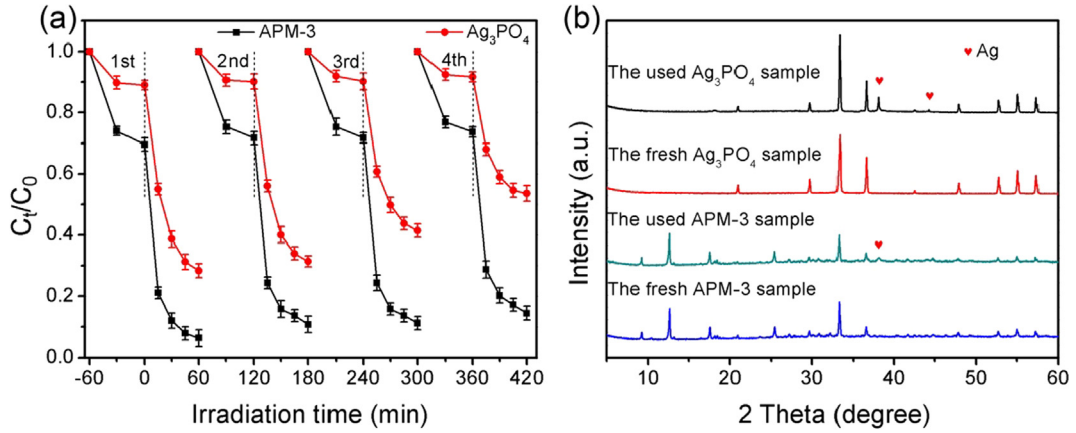

Fig. 9. (a) Cycling photocatalytic tests of Ag_3PO_4 and APM-3 for degradation of TC under visible light irradiation; (b) XRD patterns of the fresh and used Ag_3PO_4 and APM-3.

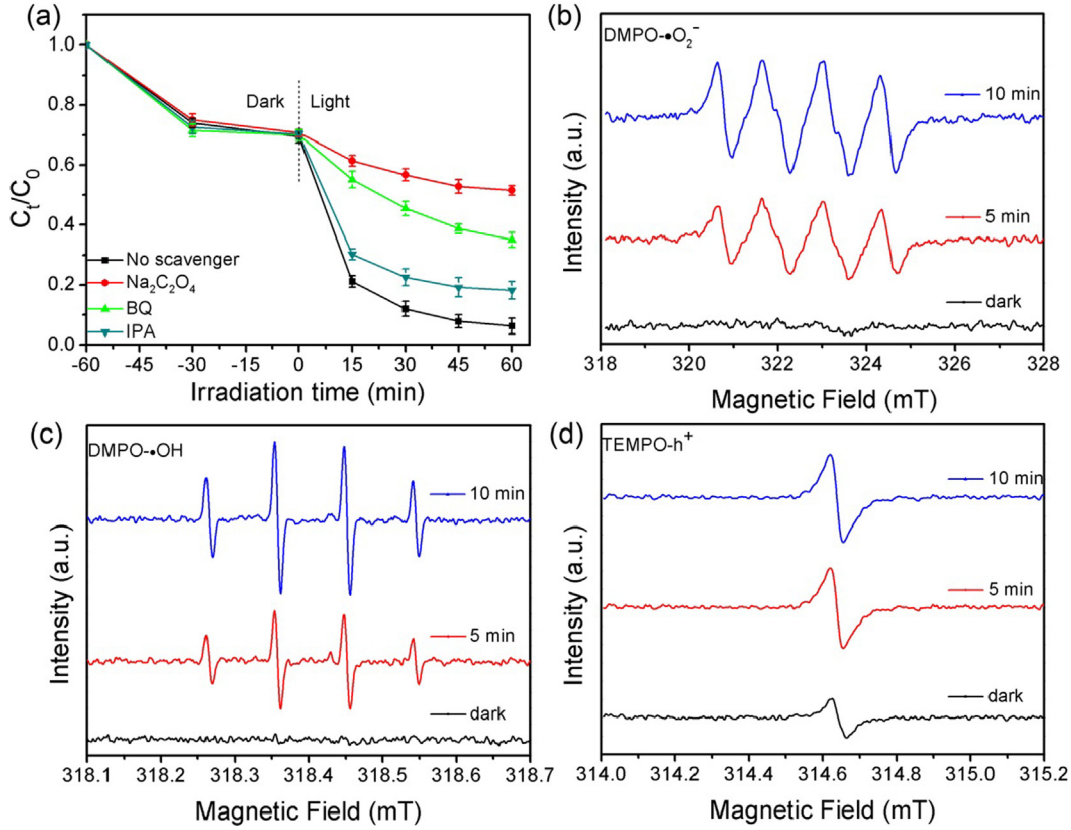

Fig. 10. (a) Photocatalytic curves of APM-3 composites with different scavengers for the degradation of TC, (b) Spin-trapping ESR spectra for APM-3 in methanol dispersion for DMPO-$^{\cdot}O_2^-$, (c) in aqueous dispersion for DMPO-$^{\cdot}$OH, (d) in aqueous dispersion for TEMPO-h^+ under both the dark and visible light irradiation.

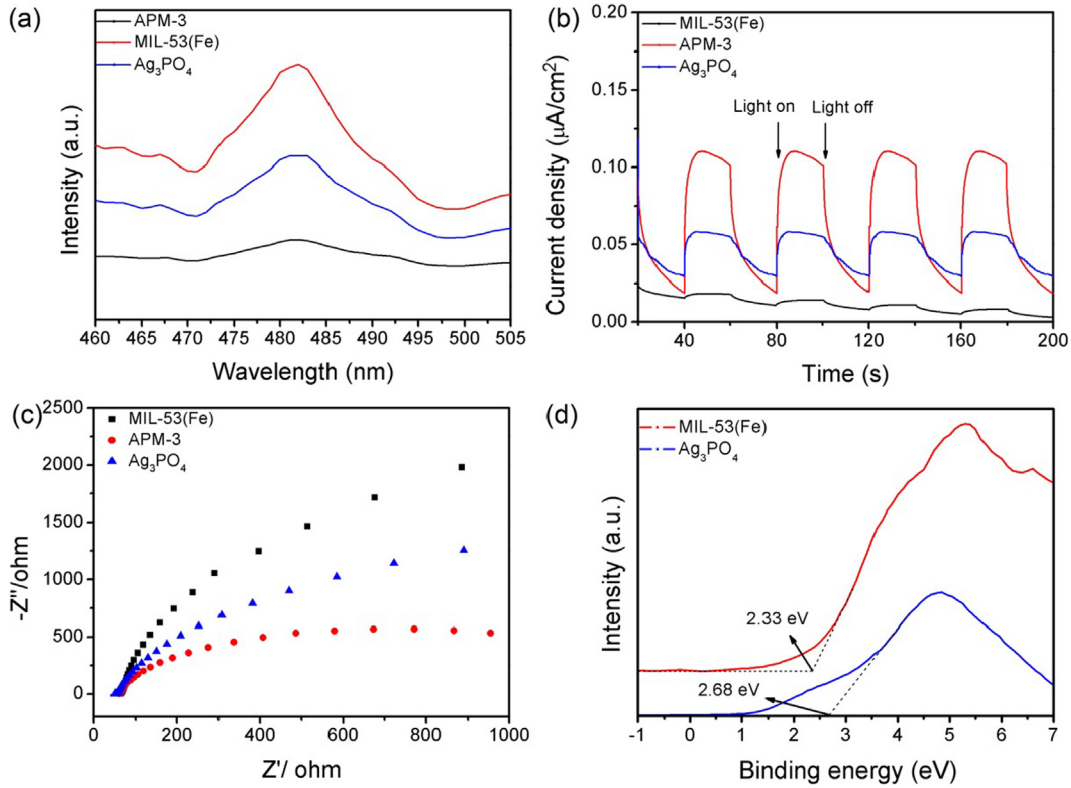

Fig. 11. (a) PL spectra, (b) Photocurrent responses, (c) EIS spectra of MIL-53(Fe), Ag_3PO_4 and APM-3, (d) VB-XPS spectra of MIL-53(Fe) and Ag_3PO_4.

recombination of charge pairs in the MIL-53(Fe) and Ag_3PO_4. Comparatively, APM-3 displayed the lowest PL signal, verifying that modify MIL-53(Fe) with Ag_3PO_4 nanoparticle can effectively separate the photoinduced electrons and holes pairs, which could make contributions to the higher photocatalytic performance.

To further study the charge separation and migration of pure MIL-53(Fe), Ag_3PO_4 and APM-3 composite, photocurrent (PC) response tests were carried out in visible light on and off cycles. All prepared electrodes were stable and the photocurrent presented good reproducibility. As displayed in Fig. 11b, nearly no signal of photocurrent response was observed over pure MIL-53(Fe), and pure Ag_3PO_4 showed weak photocurrent response under the same condition. In contrast, APM-3 exhibited the highest photocurrent intensity, which was about 3.2 times and 34.7 times as high as that of Ag_3PO_4 and MIL-53(Fe), respectively. The result inferred that APM-3 composite could generate more charges and has the highest photoinduced charge separation efficiency.

EIS measurement was another effective strategy to reflect the charge transport capability of photocatalyst. In general, the smaller arc radius of the EIS Nyquist suggests a smaller charge-transfer resistance [64]. As shown in Fig. 11c, the radius of the three samples were presented in the following order: MIL-53(Fe) > Ag_3PO_4 > APM-3, demonstrating APM-3 possessed the lowest resistance. The result was in corresponding to the analysis of PL and PC response tests.

From Fig. 4c and d, the band gap of MIL-53(Fe) and Ag_3PO_4 was calculated to be 2.74 eV and 2.26 eV, respectively. The valence band (VB) positions of MIL-53(Fe) and Ag_3PO_4 were confirmed by XPS technique. As exhibited in Fig. 11d, the E_{VB} of MIL-53(Fe) and Ag_3PO_4 was determined to be 2.33 eV and 2.68 eV. Furthermore, the conduction band (E_{CB}) of the samples could be calculated on the basis of the following equation:

$$E_{CB} = E_{VB} - E_g \quad (2)$$

As a result, the corresponding E_{CB} values of MIL-53(Fe) and Ag_3PO_4 were estimated to be −0.41 and +0.42 eV, respectively.

Based on the above theoretical analyses, two possible charge transfer ways were illustrated in Fig. 12. In the traditional electron-hole separation process (Fig. 12a), the electrons accumulated on the CB of MIL-53(Fe) would flow into the CB of Ag_3PO_4 since the CB edge potential of MIL-53(Fe) is more negative than that of Ag_3PO_4, while the holes in the VB of Ag_3PO_4 will migrate to the VB of MIL-53(Fe). In this manner, the electrons would gather to the CB of Ag_3PO_4 and the holes would accumulate on the VB of MIL-53(Fe). Despite the charges looked to be separated effectively, it was not beneficial for the electrons in Ag_3PO_4 to produce $^{\cdot}O_2^-$ through O_2 reduction because the potential of $O_2/^{\cdot}O_2^-$ (−0.33 eV vs NHE) was more negative than the CB edge potential of Ag_3PO_4 (+0.42 eV) [32]. The similar problem appeared in the holes gathered on MIL-53(Fe), which could not oxidize H_2O to form $^{\cdot}OH$ because the potential of $OH^-/^{\cdot}OH$ (+2.40 eV vs NHE) was more positive than the VB potential of MIL-53(Fe). The above discussion was in contradiction with the trapping experiment. Therefore, the traditional model was not reasonable. According to the aforementioned analysis, a possible Z-scheme mechanism for pollutants degradation over APM-3 sample was proposed as presented in Fig. 12b. When APM-3 composite was under visible light illumination, both the MIL-53(Fe) and Ag_3PO_4 could be excited and the photogenerated electrons on their VB can be transferred into their corresponding CB, leaving holes on their VB at the mean time. Moreover, metallic Ag emerged on the interface of MIL-53(Fe) and Ag_3PO_4 in the early process of visible light illumination. Ag nanoparticles can be acted as the bridge for charge transmission, and the Fermi level of metallic Ag is between the CB of Ag_3PO_4 and the VB of MIL-53(Fe) [66]. The photo-induced electrons accumulated on the CB of Ag_3PO_4 should be prone to migrate to metallic Ag via the Schottky barrier, and then transferred into the VB of MIL-53(Fe) and react with the holes there, which was more quickly than the recombination between the electrons and holes of MIL-53(Fe)

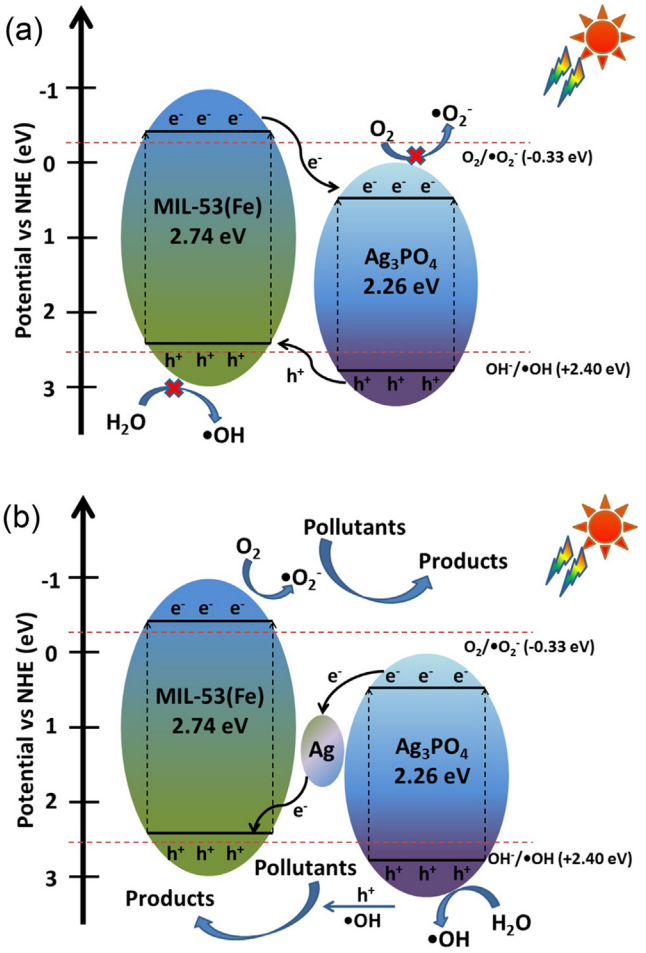

Fig. 12. Photocatalytic mechanism scheme and the possible charge separation over APM-3 composite: (a) Traditional model and (b) Z-scheme heterojunction model.

itself. Therefore, the effective charge transfer could greatly hamper the undesirable recombination of charge carriers in the photocatalytic system. The strong reductive electrons accumulated on the CB of MIL-53(Fe) and an electron-rich region could be formed, which could easily react with O_2 to generate $^{\cdot}O_2^-$ owing to the more negative CB edge potential of MIL-53(Fe) than that of $O_2/^{\cdot}O_2^-$. Simultaneously, the holes remaining on the VB of Ag_3PO_4 could produce a hole-rich region to oxidize H_2O to generate $^{\cdot}OH$ or degrade the pollutants to harmless products directly. As a result, the Z-scheme transfer system can promote the electron-hole separation effectively, which reasonably explained the excellent photocatalytic performance and photostability of APM-3 composite.

4. Conclusions

In this report, novel Ag_3PO_4/MIL-53(Fe) heterojunction hybrids were successfully fabricated via a simple in situ precipitation method. All the as-prepared Ag_3PO_4/MIL-53(Fe) composites exhibited more excellent photocatalytic performances than that of pristine catalysts for multiple antibiotics degradation under visible light illumination. The APM-3 composite displayed the best photocatalytic activity, for which the removal of antibiotics was 93.72% (TC), 90.12% (OTC), 85.54% (CTC) and 91.74% (DCL). The results of PL spectrum, photocurrent response test and EIS indicate that APM-3 possessed higher separation efficiency of photogenerated charges. A possible Z-scheme mechanism composed of MIL-53(Fe), metallic Ag and Ag_3PO_4 was proposed to reasonably explain the outstanding photocatalytic performance and

photostability of APM-3 composite. Furthermore, scavenger experiments and ESR tests verified that the active groups worked in the photocatalytic system were $^{\cdot}O_2^-$, $^{\cdot}OH$ and h^+. This work could offer a new insight to design splendid photocatalysts for environmental remediation.

Acknowledgments

This work was financially supported by National Natural Science Foundation of China (NSFC, Grant No. 51578223 and 51521006) and the Key Research and Development Program of Hunan Province (2017SK2242).

Appendix A. Supplementary data

Supplementary data to this article can be found online at https://doi.org/10.1016/j.apsusc.2018.09.144.

References

[1] A.K. Sarmah, M.T. Meyer, A.B. Boxall, A global perspective on the use, sales, exposure pathways, occurrence, fate and effects of veterinary antibiotics (VAs) in the environment, Chemosphere 65 (2006) 725–759.
[2] J. Xue, S. Ma, Y. Zhou, Z. Zhang, M. He, Facile photochemical synthesis of Au/Pt/g-C_3N_4 with plasmon-enhanced photocatalytic activity for antibiotic degradation, ACS Appl. Mater. Interf. 7 (18) (2015) 9630–9637.
[3] J. Jeong, W. Song, W.J. Cooper, J. Jung, J. Greaves, Degradation of tetracycline antibiotics: mechanisms and kinetic studies for advanced oxidation/reduction processes, Chemosphere 78 (2010) 533–540.
[4] W. Xiong, G. Zeng, Z. Yang, Y. Zhou, C. Zhang, M. Cheng, Y. Liu, L. Hu, J. Wan, C. Zhou, Adsorption of tetracycline antibiotics from aqueous solutions on nanocomposite multi-walled carbon nanotube functionalized MIL-53(Fe) as new adsorbent, Sci. Tot. Environ. 627 (2018) 235–244.
[5] X. Liu, D. Yang, Y. Zhou, J. Zhang, L. Luo, S. Meng, S. Chen, M. Tan, Z. Li, L. Tang, Electrocatalytic properties of N-doped graphite felt in electro-Fenton process and degradation mechanism of levofloxacin, Chemosphere 182 (2017) 306–315.
[6] P. Song, Z. Yang, G. Zeng, X. Yang, H. Xu, L. Wang, R. Xu, W. Xiong, K. Ahmad, Electrocoagulation treatment of arsenic in wastewaters: a comprehensive review, Chem. Eng. J. 317 (2017) 707–725.
[7] S.F. Pan, M.P. Zhu, J.P. Chen, Z.H. Yuan, L.B. Zhong, Y.M. Zheng, Separation of tetracycline from wastewater using forward osmosis process with thin film composite membrane-Implications for antibiotics recovery, Sep. Purif. Technol. 153 (2015) 76–83.
[8] C. Liang, C.G. Niu, H. Guo, D. Huang, X.J. Wen, S.F. Yang, G. Zeng, Combination of efficient charge-separation process with the assistance of novel dual Z-scheme system: self-assembly photocatalyst of Ag@AgI/BiOI modified oxygen-doped carbon nitride nanosheet with enhanced photocatalytic performance, Catal. Sci. Technol. 8 (2018) 1161–1175.
[9] C. Yang, J. Cheng, Y. Chen, Y. Hu, CdS nanoparticles immobilized on porous carbon polyhedrons derived from a metal-organic framework with enhanced visible light photocatalytic activity for antibiotic degradation, Appl. Surf. Sci. 420 (2017) 252–259.
[10] C. Zhou, C. Lai, P. Xu, G. Zeng, D. Huang, C. Zhang, M. Cheng, L. Hu, J. Wan, Y. Liu, In situ grown AgI/$Bi_{12}O_{17}Cl_2$ heterojunction photocatalysts for visible light degradation of sulfamethazine: efficiency, pathway and mechanism, ACS Sust. Chem. Eng. 6 (3) (2018) 4174–4184.
[11] Z. Xiu, H. Bo, Y. Wu, X. Hao, Graphite-like C_3N_4 modified Ag_3PO_4 nanoparticles with highly enhanced photocatalytic activities under visible light irradiation, Appl. Surf. Sci. 289 (2014) 394–399.
[12] C. Zhou, C. Lai, C. Zhang, G. Zeng, D. Huang, M. Cheng, L. Hu, W. Xiong, M. Chen, J. Wang, Y. Yang, L. Jiang, Semiconductor/boron nitride composites: synthesis, properties, and photocatalysis applications, Appl. Catal. B 238 (2018) 6–18.
[13] H. Wang, X. Yuan, H. Wang, X. Chen, Z. Wu, L. Jiang, W. Xiong, G. Zeng, Facile synthesis of Sb_2S_3/ultrathin g-C_3N_4 sheets heterostructures embedded with g-C_3N_4 quantum dots with enhanced NIR-light photocatalytic performance, Appl. Catal. B 193 (2016) 36–46.
[14] B.V. Harbuzaru, A. Corma, F. Rey, P. Atienzar, J.L. Jordá, H. García, D. Ananias, L.D. Carlos, J. Rocha, Metal-organic nanoporous structures with anisotropic photoluminescence and magnetic properties and their use as sensors, Angew. Chem. 47 (2008) 1080–1083.
[15] Y. Fu, D. Sun, Y. Chen, R. Huang, Z. Ding, X. Fu, Z. Li, An amine-functionalized titanium metal-organic framework photocatalyst with visible-light-induced activity for CO_2 reduction, Angew. Chem. 51 (2012) 3364–3367.
[16] F.X.L.I. Xamena, A. Corma, H. Garcia, Applications for metal – organic frameworks (MOFs) as quantum dot semiconductors, J. Phys. Chem. C 111 (2007) 80–85.
[17] S. Wang, X. Wang, Multifunctional metal-organic frameworks for photocatalysis, Small 11 (2015) 3097–3112.
[18] K. Meyer, M. Ranocchiari, J.A.V. Bokhoven, Metal organic frameworks for photocatalytic water splitting, Energy Environ. Sci. 8 (2015) 1923–1937.
[19] R. Li, W. Zhang, K. Zhou, Metal-organic-framework-based catalysts for photoreduction of CO_2, Adv. Mater. (2018) e1705512.
[20] X. Wang, X. Zhao, D. Zhang, G. Li, H. Li, Microwave irradiation induced UIO-66-NH_2 anchored on graphene with high activity for photocatalytic reduction of CO_2, Appl. Catal. B 228 (2018) 47–53.
[21] C. Racles, M.F. Zaltariov, M. Iacob, M. Silion, M. Avadanei, A. Bargan, Siloxane-based metal–organic frameworks with remarkable catalytic activity in mild environmental photodegradation of azo dyes, Appl. Catal. B 205 (2017) 78–92.
[22] X. Liu, Y. Zhou, J. Zhang, L. Tang, L. Luo, G. Zeng, Iron containing metal-organic frameworks: structure synthesis, and applications in environmental remediation, ACS Appl. Mater. Interf. 9 (24) (2017) 20255–20275.
[23] J.J. Du, Y.P. Yuan, J.X. Sun, F.M. Peng, X. Jiang, L.G. Qiu, A.J. Xie, Y.H. Shen, J.F. Zhu, New photocatalysts based on MIL-53 metal-organic frameworks for the decolorization of methylene blue dye, J. Hazard. Mater. 190 (2011) 945–951.
[24] R. Liang, F. Jing, L. Shen, N. Qin, L. Wu, MIL-53(Fe) as a highly efficient bifunctional photocatalyst for the simultaneous reduction of Cr(VI) and oxidation of dyes, J. Hazard. Mater. 287 (2015) 364–372.
[25] L. Ai, C. Zhang, L. Li, J. Jiang, Iron terephthalate metal–organic framework: revealing the effective activation of hydrogen peroxide for the degradation of organic dye under visible light irradiation, Appl. Catal. B Environ. 148–149 (2014) 191–200.
[26] Y. Gao, S. Li, Y. Li, L. Yao, H. Zhang, Accelerated photocatalytic degradation of organic pollutant over metal-organic framework MIL-53(Fe) under visible LED light mediated by persulfate, Appl. Catal. B 202 (2017) 165–174.
[27] W. Huang, N. Liu, X. Zhang, M. Wu, L. Tang, Metal organic framework g-C_3N_4 /MIL-53(Fe) heterojunctions with enhanced photocatalytic activity for Cr(VI) reduction under visible light, Appl. Surf. Sci. 425 (2017) 107–116.
[28] L. Hu, G. Deng, W. Lu, S. Pang, X. Hu, Deposition of CdS nanoparticles on MIL-53(Fe) metal-organic framework with enhanced photocatalytic degradation of RhB under visible light irradiation, Appl. Surf. Sci. 410 (2017) 401–413.
[29] C. Zhang, K. Yu, Y. Feng, Y. Chang, T. Yang, Y. Xuan, D. Lei, L.L. Lou, S. Liu, Novel 3DOM-$SrTiO_3$/Ag/Ag_3PO_4 ternary Z-scheme photocatalysts with remarkably improved activity and durability for contaminant degradation, Appl. Catal. B 210 (2017) 77–87.
[30] L. Zhou, W. Zhang, L. Chen, H. Deng, Z-scheme mechanism of photogenerated carriers for hybrid photocatalyst Ag_3PO_4/g-C_3N_4 in degradation of sulfamethoxazole, J. Coll. Interf. Sci. 487 (2016) 410–417.
[31] F. Chen, Q. Yang, J. Sun, F. Yao, S. Wang, Y. Wang, X. Wang, X. Li, C. Niu, D. Wang, Enhanced photocatalytic degradation of tetracycline by AgI/$BiVO_4$ heterojunction under visible-light irradiation: mineralization efficiency and mechanism, ACS Appl. Mater. Interf. 8 (48) (2016) 32887–32900.
[32] F. Chen, Q. Yang, F. Yao, S. Wang, J. Sun, H. An, K. Yi, Y. Wang, Y. Zhou, L. Wang, X. Li, D. Wang, G. Zeng, Visible-light photocatalytic degradation of multiple antibiotics by AgI nanoparticle-sensitized Bi_5O_7I microspheres: enhanced interfacial charge transfer based on Z-scheme heterojunctions, J. Catal. 352 (2017) 160–170.
[33] Z. Yi, J. Ye, N. Kikugawa, T. Kako, S. Ouyang, H. Stuartwilliams, H. Yang, J. Cao, W. Luo, Z. Li, An orthophosphate semiconductor with photooxidation properties under visible-light irradiation, Nat. Mater. 9 (7) (2010) 559–564.
[34] N. Guo, H. Li, X. Xu, H. Yu, Hierarchical Fe_3O_4@MoS_2/Ag_3PO_4 magnetic nanocomposites: enhanced and stable photocatalytic performance for water purification under visible light irradiation, Appl. Surf. Sci. 389 (2016) 227–239.
[35] T. Cai, Y. Liu, L. Wang, S. Zhang, Y. Zeng, J. Yuan, J. Ma, W. Dong, C. Liu, S. Luo, Silver phosphate-based Z-Scheme photocatalytic system with superior sunlight photocatalytic activities and anti-photocorrosion performance, Appl. Catal. B 208 (2017) 1–13.
[36] T. Yan, J. Tian, W. Guan, Z. Qiao, W. Li, J. You, B. Huang, Ultra-low loading of Ag_3PO_4 on hierarchical In_2S_3 microspheres to improve the photocatalytic performance: the cocatalytic effect of Ag and Ag_3PO_4, Appl. Catal. B 202 (2016) 84–94.
[37] P. Horcajada, C. Serre, G. Maurin, N.A. Ramsahye, F. Balas, M. Vallet-Regí, M. Sebban, F. Taulelle, G. Férey, Flexible porous metal-organic frameworks for a controlled drug delivery, JACS 130 (2008) 6774–6780.
[38] F. Millange, N. Guillou, R.I. Walton, J.M. Grenèche, I. Margiolaki, G. Férey, Effect of the nature of the metal on the breathing steps in MOFs with dynamic frameworks, Chem. Commun. 39 (39) (2008) 4732–4734.
[39] W. Xiong, Z. Zeng, X. Li, G. Zeng, R. Xiao, Z. Yang, Y. Zhou, C. Zhang, M. Cheng, L. Hu, C. Zhou, L. Qin, R. Xu, Y. Zhang, Multi-walled carbon nanotube/amino-functionalized MIL-53(Fe) composites: Remarkable adsorptive removal of antibiotics from aqueous solutions, Chemosphere 210 (2018) 1061–1069.
[40] C. Zhang, L. Ai, J. Jiang, Graphene hybridized photoactive iron terephthalate with enhanced photocatalytic activity for the degradation of rhodamine B under visible light, Ind. Eng. Chem. Res. 54 (2015) 153–163.
[41] A. Banerjee, R. Gokhale, S. Bhatnagar, J. Jog, M. Bhardwaj, B. Lefez, B. Hannoyer, S. Ogale, MOF derived porous carbon–Fe_3O_4 nanocomposite as a high performance, recyclable environmental superadsorbent, J. Mater. Chem. 22 (2012) 19694–19699.
[42] C. Gong, D. Chen, X. Jiao, Q. Wang, Continuous hollow α-Fe_2O_3 and α-Fe fibers prepared by the sol–gel method, J. Mater. Chem. 12 (2002) 1844–1847.
[43] F.J. Zhang, F.Z. Xie, S.F. Zhu, J. Liu, J. Zhang, S.F. Mei, W. Zhao, A novel photofunctional g-C_3N_4/Ag_3PO_4 bulk heterojunction for decolorization of Rh.B, Chem. Eng. J. 228 (2013) 435–441.
[44] S. Tam, J. Dusseault, S.M. Menard, J. Halle, L. Yahia, Physicochemical model of alginate-poly-L-lysine microcapsules defined at the micrometric/nanometric scale using ATR-FTIR, XPS, and ToF-SIMS, Biomaterials 26 (2005) 6950–6961.
[45] C. Yu, L. Gou, X. Zhou, N. Bao, H. Gu, Chitosan–FeO nanocomposite based electrochemical sensors for the determination of bisphenol A, Electrochim. Acta 56 (2011) 9056–9063.
[46] S. Sepúlveda-Guzmán, L. Lara, O. Pérez-Camacho, O. Rodríguez-Fernández,

A. Olivas, R. Escudero, Synthesis and characterization of an iron oxide poly(styrene-co-carboxybutylmaleimide) ferrimagnetic composite Polymer, Polymer 48 (2007) 720–727.
[47] R. Liang, F. Jing, L. Shen, N. Qin, L. Wu, MIL-53(Fe) as a highly efficient bifunctional photocatalyst for the simultaneous reduction of Cr(VI) and oxidation of dyes, J. Hazard. Mater. 287C (2015) 364–372.
[48] Q. Li, F. Wang, Y. Hua, Y. Luo, X. Liu, G. Duan, X. Yang, Deposition-precipitation preparation of $Ag/Ag_3PO_4/WO_3$ nanocomposites for efficient visible-light degradation of rhodamine B under strongly acidic/alkaline conditions, J. Coll. Interf. Sci. 506 (2017) 207–216.
[49] M. Pu, Z. Guan, Y. Ma, J. Wan, Y. Wang, M.L. Brusseau, H. Chi, Synthesis of iron-based metal-organic framework MIL-53 as an efficient catalyst to activate persulfate for the degradation of Orange G in aqueous solution, Appl. Catal. A 549 (2017) 82–92.
[50] K. Matsuyama, N. Hayashi, M. Yokomizo, T. Kato, K. Ohara, T. Okuyama, Supercritical carbon dioxide-assisted drug loading and release from biocompatible porous metal-organic frameworks, J. Mater. Chem. B 2 (2014) 7551–7558.
[51] Q. Sun, M. Liu, K. Li, Y. Zuo, Y. Han, J. Wang, C. Song, G. Zhang, X. Guo, Facile synthesis of Fe-containing metal organic framework as highly efficient catalyst for degradation of phenol at neutral pH and ambient temperature, Cryst. Eng. Commun. 17 (2015) 7160–7168.
[52] R. Panda, S. Rahut, J.K. Basu, Preparation of a Fe_2O_3/MIL-53(Fe) composite by partial thermal decomposition of MIL-53(Fe) nanorods and their photocatalytic activity, RSC Adv. 6 (2016) 80981–80985.
[53] P. Cervini, L.C.M. Machado, A.P.G. Ferreira, B. Ambrozini, É.T.G. Cavalheiro, Thermal decomposition of tetracycline and chlortetracycline, J. Anal. Appl. Pyrol. 118 (2016) 317–324.
[54] G.T. Vuong, M.H. Pham, Direct synthesis and mechanism of the formation of mixed metal Fe_2Ni-MIL-88B, Cryst. Eng. Commun. 15 (2013) 9694–9703.
[55] W. Cao, Z. Gui, L. Chen, X. Zhu, Z. Qi, Facile synthesis of sulfate-doped Ag_3PO_4 with enhanced visible light photocatalystic activity, Appl. Catal. B 200 (2017) 681–689.
[56] Z. Yang, X. Xu, X. Liang, C. Lei, Y. Wei, P. He, B. Lv, H. Ma, Z. Lei, MIL-53(Fe)-graphene nanocomposites: efficient visible-light photocatalysts for the selective oxidation of alcohols, Appl. Catal. B 198 (2016) 112–123.
[57] R. Xu, Z.H. Yang, Q.P. Wang, Y. Bai, J.B. Liu, Y. Zheng, Y.R. Zhang, W.P. Xiong, K. Ahmad, C.Z. Fan, Rapid startup of thermophilic anaerobic digester to remove tetracycline and sulfonamides resistance genes from sewage sludge, Sci. Total Environ. 612 (9) (2017) 788–798.
[58] Y. Yang, Z. Zeng, C. Zhang, D. Huang, G. Zeng, R. Xiao, C. Lai, C. Zhou, H. Guo, W. Xue, Construction of iodine vacancy-rich BiOI/Ag@AgI Z-scheme heterojunction photocatalysts for visible-light-driven tetracycline degradation: transformation pathways and mechanism insight, Chem. Eng. J. 349 (2018) 808–821.
[59] J. Cao, Z.-H. Yang, W.-P. Xiong, Y.-Y. Zhou, Y.-R. Peng, X. Li, C.-Y. Zhou, R. Xu, Y.-R. Zhang, One-step synthesis of Co-doped UiO-66 nanoparticle with enhanced removal efficiency of tetracycline: simultaneous adsorption and photocatalysis, Chem. Eng. J. 353 (2018) 126–137.
[60] R. Hailili, Z.Q. Wang, M. Xu, Y. Wang, X.Q. Gong, T. Xu, C. Wang, Layered nanostructured ferroelectric perovskite $Bi_5FeTi_3O_{15}$ for visible light photodegradation of antibiotics, J. Mater. Chem. A 5 (40) (2017) 21275–21290.
[61] X. Liu, L. Huang, X. Wu, Z. Wang, G. Dong, C. Wang, Y. Liu, L. Wang, $Bi_2Zr_2O_7$ nanoparticles synthesized by soft-templated sol-gel methods for visible-light-driven catalytic degradation of tetracycline, Chemosphere 210 (2018) 424–432.
[62] Y.-Y. Chen, Y.-L. Ma, J. Yang, L.-Q. Wang, J.-M. Lv, C.-J. Ren, Aqueous tetracycline degradation by H_2O_2 alone: removal and transformation pathway, Chem. Eng. J. 307 (2017) 15–23.
[63] H. Dong, Z. Jiang, C. Zhang, J. Deng, K. Hou, Y. Cheng, L. Zhang, G. Zeng, Removal of tetracycline by Fe/Ni bimetallic nanoparticles in aqueous solution, J. Coll. Interf. Sci. 513 (2018) 117–125.
[64] C. Liang, C.G. Niu, M. Shen, S.F. Yang, G. Zeng, Controllable fabrication of novel heterojunction composite: AgBr and $Ag@Ag_2O$ co-modified Ag_2CO_3 with excellent photocatalytic performance towards refractory pollutants degradation, New J. Chem. 42 (5) (2018) 3270–3281.
[65] C. Zhou, C. Lai, D. Huang, G. Zeng, C. Zhang, M. Cheng, L. Hu, J. Wan, W. Xiong, M. Wen, Highly porous carbon nitride by supramolecular preassembly of monomers for photocatalytic removal of sulfamethazine under visible light driven, Appl. Catal. B 220 (2017) 202–210.
[66] C. Liang, C.G. Niu, X.J. Wen, S.F. Yang, M.C. Shen, G.M. Zeng, Effective removal of colourless pollutants and organic dyes by Ag@AgCl nanoparticle-modified $CaSn(OH)_6$ composite under visible light irradiation, New J. Chem. 41 (13) (2017) 5334–5346.